THE JOURNAL OF PHYSICAL CHEMISTRY A

ARTICLE

pubs.acs.org/JPCA

Does $\hbar$ Play a Role in Multidimensional Spectroscopy? Reduced Hierarchy Equations of Motion Approach to Molecular Vibrations†

Atsunori Sakurai and Yoshitaka Tanimura*

Department of Chemistry, Graduate School of Science, Kyoto Universiy, Kyoto 606-8502, Japan

ABSTRACT: To investigate the role of quantum effects in vibrational spectroscopies, we have carried out numerically exact calculations of linear and nonlinear response functions for an anharmonic potential system nonlinearly coupled to a harmonic oscillator bath. Although one cannot carry out the quantum calculations of the response functions with full molecular dynamics (MD) simulations for a realistic system which consists of many molecules, it is possible to grasp the essence of the quantum effects on the vibrational spectra by employing a model Hamiltonian that describes an intra- or intermolecular vibrational motion in a condensed phase. The present model fully includes vibrational relaxation, while the stochastic model often used to simulate infrared spectra does not. We have employed the reduced quantum hierarchy equations of motion approach in the Wigner space representation to deal with nonperturbative, non-Markovian, and nonsecular system−bath interactions. Taking the classical limit of the hierarchy equations of motion, we have obtained the classical equations of motion that describe the classical dynamics under the same physical conditions as in the quantum case. By comparing the classical and quantum mechanically calculated linear and multidimensional spectra, we found that the profiles of spectra for a fast modulation case were similar, but different for a slow modulation case. In both the classical and quantum cases, we identified the resonant oscillation peak in the spectra, but the quantum peak shifted to the red compared with the classical one if the potential is anharmonic. The prominent quantum effect is the 1−2 transition peak, which appears only in the quantum mechanically calculated spectra as a result of anharmonicity in the potential or nonlinearity of the system−bath coupling. While the contribution of the 1−2 transition is negligible in the fast modulation case, it becomes important in the slow modulation case as long as the amplitude of the frequency fluctuation is small. Thus, we observed a distinct difference between the classical and quantum mechanically calculated multidimensional spectra in the slow modulation case where spectral diffusion plays a role. This fact indicates that one may not reproduce the experimentally obtained multidimensional spectrum for high-frequency vibrational modes based on classical molecular dynamics simulations if the modulation that arises from surrounding molecules is weak and slow. A practical way to overcome the difference between the classical and quantum simulations was discussed.

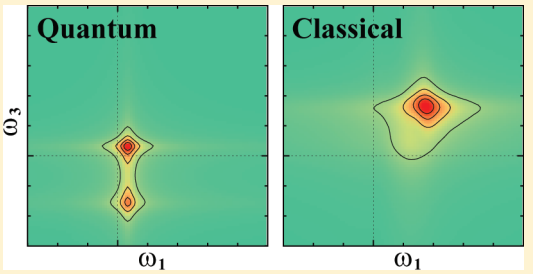

1. INTRODUCTION

Spectral line shapes contain important information about inter- and intramolecular dynamics in the condensed phase.[1] Since molecular vibrational motions are extremely fast, femtosecond laser spectroscopy is necessary to investigate the dynamics of vibrational motion. Energy and phase relaxation, as well as thermal excitations, take place whenever a system is affected by coupling to other degrees of freedom. The resultant line shape from molecules in the condensed phase is broadened, and several peaks often overlap. Multidimensional spectroscopy is a powerful means of analyzing the complex molecular dynamics.[2] Molecular dynamics (MD) simulations are useful for analyzing the experimental results, since they can access the details of molecular interactions that change dynamically through molecular configurations.[3−12] It is essential to calculate the optical response functions quantum mechanically for a case where the thermal energy is small compared to the relevant splitting energy. Due to the complexity of the system, the calculations of the linear and nonlinear response functions with full MD simulations are limited to classical dynamics. Quantum dynamical treatments such as centroid dynamics[13] and mixed quantum-classical dynamics[14,15] are computationally expensive and cannot easily be applied to calculate the linear and nonlinear spectra. Alternatively, the linear and nonlinear spectra can be calculated by adapting the response function formalism using parameters obtained from classical MD simulations.[16−26] These methods mostly neglect vibrational relaxation beyond the initial ground state. Inclusion of many optical modes with complex mode coupling is not so easy. All approaches developed so far are based on some approximations, and justification for the calculated results is necessary. Although we

† Part of the "Graham R. Fleming Festschrift".

Special Issue: Graham R. Fleming Festschrift

Received: October 5, 2010
Revised: December 13, 2010
Published: January 19, 2011

can compare the calculated spectra with experimentally obtained spectra, the quantum effects cannot be isolated from classical effects, since they are experimentally inseparable. In addition, we should be aware of the possibility that vibrational spectroscopy may not be sensitive for quantum effects. The well-known quantum effect for vibrational motion is the zero-point oscillation; however, the contribution from the zero-point energy may not be important in vibrational spectroscopy. This can be seen from the linear absorption signal of a harmonic oscillator system. The quantum and classical expressions of the signal are given by

$$R_{\mathrm{qm}}^{(1)}(t) = i\langle[\mu(t),\mu]\rangle/\hbar$$

and

$$R_{\mathrm{cl}}^{(1)}(t) = \langle[\mu(t),\mu]\rangle$$

respectively. If we calculate both signals for a harmonic oscillator system with the frequency ω_0 and the molecular coordinate q, we have the same result as $\mu_1^2 \sin(\omega_0 t)$, where $\mu(q) = \mu_1 q$ is the molecular dipole. The zero-point energy does not play any role in vibrational spectroscopy if the potential is harmonic. This is because the resonant frequency in the quantum case is determined by the difference between the energy eigenvalues rather than the eigenvalue itself and the contributions from the zero-point energy are canceled. This indicates that even if we carry out the exact quantum calculations, quantum effects may not appear in vibrational spectra. Identification of the quantum effects is thus difficult even when we have accurate simulation and experimental results on hand.

The best way to identify quantum effects in vibrational spectra is to compare the signals calculated from exact classical simulations with those from exact quantum simulations. While the comparisons of the quantum and classical simulation results are easily made for an isolated molecular system where the regular Schrödinger and Newtonian formalisms are applied, they are difficult for a system in a condensed phase, since quantum equations of motion to meet the physical conditions necessary to calculate the vibrational spectra have not been fully developed. Several attempts have been made to justify using classical or semiclassical simulations to interpret experimental results.[27−31] Although one cannot carry out fully quantum mechanical calculations for a realistic system which consists of many molecules, it is possible to grasp the essence of the quantum effects on the vibrational spectra by employing a model Hamiltonian that describes an intra- or intermolecular vibrational motion in the condensed phase.

For this purpose, we consider a single anharmonic oscillator system nonlinearly coupled to a harmonic heat bath.[32] This model contains the essence of condensed dissipative dynamics for vibrational spectroscopy; after a long time evolution period, the system approaches to the quantum thermal equilibrium state as a result of the fluctuations and dissipation with vibrational dephasing arising from the heat bath. Thus, the present model fully includes vibrational relaxation, while the stochastic model often used to simulate infrared spectra does not. Markovian, perturbative, and secular approximations are avoided, since the vibrational spectrum is very sensitive to such approximations. So far, only the hierarchy equation approach[33−40] and the real-time path integral approach[41] can handle the quantum dissipative dynamics for multidimensional spectroscopy to the desired accuracy. In this paper, we employ the quantum and classical hierarchy equations of motion in the Wigner space representation to investigate the role of quantum dynamics and to explore the validity of classical molecular dynamics simulations for linear and nonlinear vibrational spectroscopies.

This paper is organized as follows: In section 2, we introduce the quantum and classical hierarchy equations of motion applicable to high-frequency intramolecular vibrational mode. We then give a brief review of methodology to calculate linear and nonlinear optical responses in section 3. In section 4, some of the details for numerical simulations are described. Numerical results are presented as linear absorption and 2D-IR spectra in sections 5 and 6, respectively, and the difference between the classical and quantum results is discussed. Section 7 is devoted to concluding remarks.

2. REDUCED HIERARCHY EQUATIONS OF MOTION IN A PHASE SPACE REPRESENTATION

We consider a model that describes a classical or quantum vibration in a condensed phase environment, represented by the Hamiltonian[42−44]

$$\hat{H}_{\mathrm{tot}} = \frac{\hat{p}^2}{2m} + U(\hat{q}) + \sum_j \left[\frac{\hat{p}_j^{\,2}}{2m_j} + \frac{1}{2} m_j \omega_j^{\,2} \left(\hat{x}_j - \frac{c_j V(\hat{q})}{m_j \omega_j^{\,2}}\right)\right] \tag{1}$$

where m, $\hat{q}$, $\hat{p}$, and $U(\hat{q})$ denote the reduced mass, coordinate, momentum, and the potential of the optically active oscillator mode, respectively. An ensemble of optically inactive modes is assumed as a heat bath. The mass, coordinate, momentum, and frequency of the jth bath oscillator are given by m_j, $\hat{x}_j$, $\hat{p}_j$, and ω_j, respectively. In eq 1, the system−bath interaction is expressed as

$$\hat{H}_I = -\sum_j c_j \hat{x}_j V(\hat{q})$$

where c_j denotes the coupling strength between the system and the jth bath mode and $V(\hat{q})$ is a function of the system coordinate whose dimension is the same as $\hat{q}$. We consider only the linear dependence on the bath mode $\hat{x}_j$; however, coupling up to the second order in the vibrational mode $\hat{q}$ is included as[32−40,45−50]

$$V(\hat{q}) = V_{\mathrm{LL}}\hat{q} + \frac{1}{2} V_{\mathrm{SL}}\hat{q}^2 \tag{2}$$

We refer to the term proportional to V_{LL} as the linear−linear (LL) coupling term and the term proportional to V_{SL} as the square−linear (SL) coupling term.[45] As shown in Figure 1, the LL coupling swings and deforms the potential, whereas SL coupling alters the curvature of the potential. Hence, the LL coupling causes energy relaxation with some frequency fluctuations, while the SL coupling induces frequency fluctuations with some energy relaxation. Note that we introduced the counter term $\sum_j c_j^{\,2} V(\hat{q})^2/2m_j\omega_j^{\,2}$ to maintain the translation symmetry of the Hamiltonian for $U(\hat{q}) = 0$.[42−44]

The bath dynamics can be characterized by the spectral distribution function defined by

$$J(\omega) = \sum_j c_j^{\,2} \delta(\omega - \omega_j)/2m_j\omega_j$$

We consider the Ohmic form with the Lorentzian cutoff[33,51]

$$J(\omega) = \frac{m\zeta}{\pi} \frac{\gamma^2\omega}{\gamma^2 + \omega^2} \tag{3}$$

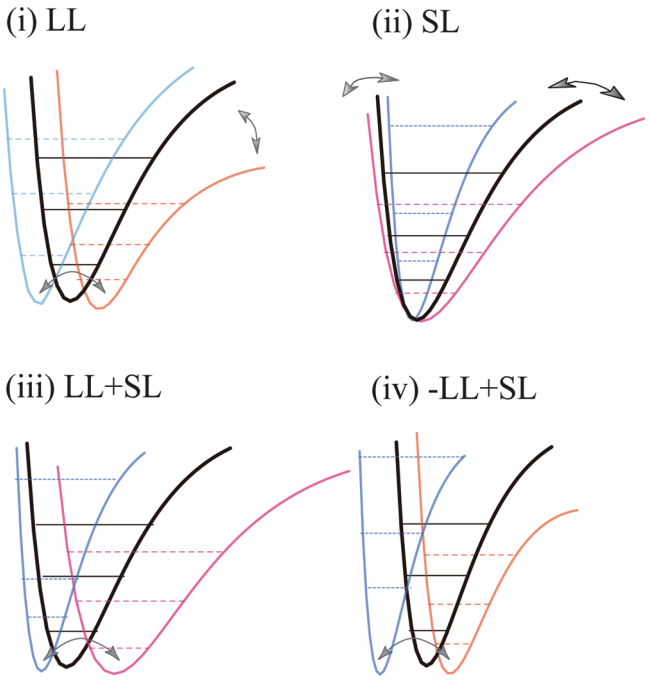

Figure 1. Schematic illustrations of effects of (i) the linear−linear (LL), (ii) the square−linear (SL), (iii) the linear−linear + square−linear (LL+SL), and (iv) the −linear−linear + square−linear (−LL+SL), system−bath couplings on an anharmonic potential. The black lines represent the unperturbed potential, while the colored lines the perturbed ones. The LL coupling interaction swings and deforms the potential, whereas the SL coupling interaction alters the curvature of the potential. In the anharmonic case, the LL coupling interaction causes energy relaxation and some frequency fluctuations, while the SL interaction causes frequency fluctuations and some energy relaxation. Since the Morse potential is not symmetric and spread to the positive direction, the potential becomes wide for additive deformation and the frequency fluctuation case (LL+SL), whereas the potential becomes narrow for the negative case (−LL+SL). Note that the LL and SL couplings mainly cause the one- and two-quantum transitions, respectively[39].

Here, γ represents the width of the spectral distribution of the bath modes and is related to the correlation time of the noise induced by the bath $\tau_c = 1/\gamma$, $\beta = 1/k_BT$ is the inverse temperature, and ζ is the system−bath coupling strength. The symmetrized correlation function of the collective bath coordinate $\hat{X} = \sum_j c_j \hat{x}_j$ in the high temperature case ($\beta\hbar\gamma \ll 1$) is then given by

$$\frac{1}{2}\langle \hat{X}(t)\hat{X}(0) + \hat{X}(0)\hat{X}(t)\rangle_B = \frac{m\zeta\gamma}{\beta} e^{-\gamma|t|} \qquad (4)$$

where $\langle \cdots \rangle_B$ represents the thermal average over the bath modes. Since ζ can be included in V_{LL}, and V_{SL} in eq 2, the effect of the system−bath interaction can be characterized by a set of four parameters, namely, β, γ, V_{LL}, and V_{SL}. While the linear−linear interaction (LL) mainly contributes to energy relaxation for the fast modulation case, the square−linear (SL) system−bath interaction leads to the vibrational dephasing for the slow modulation case due to the frequency fluctuation of system vibrations.[32−40,45−47] The LL and SL couplings also cause the one- and two-quantum transitions, respectively, as can be seen from the system−bath coupling expressed by the one-quantum creation and annihilation operators.[33−35]

The bath effects consist of the fluctuation and dissipation parts, both of which ensure the thermal equilibrium state of the entire system through the fluctuation−dissipation theorem. Note that a stochastic treatment of vibrational dephasing neglects the dissipation part of the bath effects, so that the system does not reach the thermal equilibrium state as the steady state. The validity of the stochastic treatments are assessed by comparing the nonlinear spectra calculated from the total Hamiltonian with those from the effective stochastic Hamiltonian.[32,39]

As was shown by Tanimura et al., such a dissipative system can be treated by utilizing a tridiagonal hierarchy of equations.[33−38,51−53] At a low temperature, the structure of the hierarchy becomes complicated because of the quantum nature of the heat bath characterized by Matsubara frequencies.[54] However, there is a rigorous but simple way to terminate the hierarchy with including low-temperature correction terms.[55−58] The key to calculating linear and nonlinear response functions is quantum coherence between the system and the bath, which plays an essential role for the strong system−bath coupling.[59]

To derive the equation of motion for the relevant system, we use the reduced density operator of the system by tracing over the bath degrees of freedom

$$\hat{\rho}(t) = Tr_B\{\hat{\rho}_{tot}(t)\}$$

We write the reduced density matrix $\rho(q,q';t)$ in the Wigner representation defined as[60]

$$W(p,q;t) \equiv \frac{1}{2\pi\hbar}\int_{-\infty}^{\infty} dr e^{ipr/\hbar}\rho\left(q - \frac{r}{2}, q + \frac{r}{2}; t\right) \qquad (5)$$

The Wigner distribution function is the quantum analogue of the classical distribution function in phase space. If we take the classical limit $\hbar \to 0$, the Wigner distribution function corresponds to the classical distribution function. If the noise correlation is very short ($\gamma \to \infty$) and the temperature is high (i.e., white noise, Markovian approximation), one can derive the quantum Fokker−Planck equation in a similar form as the Kramers equation.[42,61−63] In the present case, however, we cannot employ the white noise approximation since the quantum effects play a dominant role in the low temperature regime ($\beta\hbar\omega_0 > 1$) and the bath modulations are non-Markovian on the femtosecond time scale relevant to ultrafast nonlinear spectroscopy. As shown in ref 39, the dynamics of the reduced density operator for the system eq 1 is described by the quantum Fokker−Planck equation with low-temperature correction terms. In the Wigner representation, the equations of motion are expressed in the hierarchy form as

$$\frac{\partial}{\partial t} W^{(n)}_{j_1,j_2,\ldots,j_K} = -[\hat{L}_{qm} + \hat{\Xi}' + n\gamma + \sum_{k=1}^{K} j_k\nu_k]W^{(n)}_{j_1,j_2,\ldots,j_K}$$
$$+ \hat{\Phi}[W^{(n+1)}_{j_1,j_2,\ldots,j_K} + \sum_{k=1}^{K} W^{(n)}_{j_1,\ldots,(j_k+1),\ldots,j_K}] + n\hat{\Theta}_0 W^{(n-1)}_{j_1,j_2,\ldots,j_K}$$
$$+ \sum_{k=1}^{K} j_k\hat{\Theta}_k W^{(n)}_{j_1,\ldots,(j_k-1),\ldots,j_K} \qquad (6)$$

for non-negative integers $n,j_1,\ldots,j_K$, where we chose K such that $\nu_K \gg \omega_c$ for Bosonic Matsubara frequencies $\nu_k = 2\pi k/(\beta\hbar)$. To obtain eq 6, we employed the influence functional in the partial time derivative form to remove the counter term. Note that, for a

strong SL interaction at low temperature case, eq 6 associates with additional higher order hierarchy members such as $W_{j_1 j_2,\ldots,j_K}$.[64] In eq 6, $-\hat{L}_{qm}$ is the quantum Liouvillian of the system defined by[61]

$$-\hat{L}_{qm}W(p,q) \equiv -\frac{p}{m}\frac{\partial}{\partial q}W(p,q) - \frac{1}{\hbar}\int_{-\infty}^{\infty}\frac{dp'}{2\pi\hbar}U_W(p-p',q)W(p',q) \quad (7)$$

with

$$U_W(p,q) \equiv 2\int_0^{\infty} dr \sin\left(\frac{pr}{\hbar}\right)\left[U\left(q+\frac{r}{2}\right)-U\left(q-\frac{r}{2}\right)\right] \quad (8)$$

The operators $\hat{\Phi}$, $\hat{\Theta}_k$, and $\hat{\Xi}'$ are the bath-induced relaxation operators defined by

$$\hat{\Phi} \equiv -(V_{LL}+V_{SL}q)\frac{\partial}{\partial p} \quad (9)$$

$$\hat{\Theta}_0 \equiv \zeta\gamma(V_{LL}+V_{SL}q)\left[p+\frac{m\hbar\gamma}{2}\cot\left(\frac{\beta\hbar\gamma}{2}\right)\frac{\partial}{\partial p}\right] \quad (10)$$

and

$$\hat{\Theta}_k \equiv -\frac{m\zeta}{\beta}\frac{2(\beta\hbar\gamma)^2}{(2\pi k)^2-(\beta\hbar\gamma)^2}(V_{LL}+V_{SL}q)\frac{\partial}{\partial p} \quad (11)$$

for $k > 0$ and

$$\hat{\Xi}' \equiv \frac{m\zeta}{\beta}\left[1-\frac{\beta\hbar\gamma}{2}\cot\left(\frac{\beta\hbar\gamma}{2}\right)-\sum_{k=1}^{K}\frac{2(\beta\hbar\gamma)^2}{(2\pi k)^2-(\beta\hbar\gamma)^2}\right] \times (V_{LL}+V_{SL}q)^2\frac{\partial^2}{\partial p^2} \quad (12)$$

Here, N satisfies $N \equiv n+\sum_{k=1}^{K} j_k \gg \omega_c/\min(\gamma,\nu_1)$. Note that only $W_{0,\ldots,0}^{(0)}(p,q;t) \equiv W(p,q;t)$ has a physical meaning, and the other elements $W_{j_1,\ldots,j_K}^{(n)}(p,q;t)$ for $(n;j_1,\ldots,j_K) \neq (0;0,\ldots,0)$ are the auxiliary operators being introduced to avoid the explicit treatment of the inherent memory effects during the time evolution of the reduced density matrix.[33] The hierarchical given by eq 6 continues indefinitely. However, for large N, we can terminate the equations as[55]

$$\frac{\partial}{\partial t}W_{j_1 j_2,\ldots,j_K}^{(n)} = -(\hat{L}_{qm}+\hat{\Xi}')W_{j_1 j_2,\ldots,j_K}^{(n)} \quad (13)$$

This formalism is suitable for a low-temperature system ($\beta\hbar\omega_c \gg 1$ and $\beta\hbar\gamma \gg 1$) strongly coupled to the heat bath without employing the rotating wave approximation (RWA) for the system−bath interaction. The energy eigenstate representation of the above equations is given in ref 39, and briefly summarized in Appendix A.

The classical equations of motion can be deduced by taking the classical limit $\hbar \to 0$ of eq 6 and are given by[33−37,52,53]

$$\frac{\partial}{\partial t}W^{(n)} = -(\hat{L}_{cm}+n\gamma)W^{(n)}+\hat{\Phi}W^{(n+1)}+n\hat{\Theta}W^{(n-1)} \quad (14)$$

where the quantum Liouvillian eq 7 and hierarchy operator eq 10 become

$$-\hat{L}_{cm} = -\frac{p}{m}\frac{\partial}{\partial q}+\frac{\partial U(q)}{\partial q}\frac{\partial}{\partial p} \quad (15)$$

and

$$\hat{\Theta} \equiv \zeta\gamma(V_{LL}+V_{SL}q)\left(p+\frac{m}{\beta}\frac{\partial}{\partial p}\right) \quad (16)$$

respectively. Instead of eq 13, we employ the following terminator

$$\frac{\partial}{\partial t}W^{(N)} = -(\hat{L}_{cm}+N\gamma)W^{(N)}+\frac{1}{\gamma}\hat{\Phi}\hat{\Theta}W^{(N)}+N\hat{\Theta}W^{(N-1)} \quad (17)$$

which reduces to the Kramers equation for $N \to 0$ with $V_{SL} = 0$.[65,66]

3. LINEAR AND NONLINEAR OPTICAL RESPONSE FUNCTIONS

We consider a molecular system is interacting with a laser field, $E(t)$. For resonant IR spectroscopy, the Hamiltonian including the laser interaction is given by $H_{IR} = H_{tot} - \mu(\hat{q})E(t)$, where $\mu(\hat{q})$ is the dipole moment. In the first-order IR experiment, the system interacts with one pulse, whereas in the third-order IR experiments, the system interacts with three pulses. The response functions are expressed in terms of the dipole operator as[1]

$$R^{(1)}(t_1) = \frac{i}{\hbar}\mathrm{Tr}\{[\hat{\mu}(t_1),\hat{\mu}(0)]\hat{\rho}_{tot}^{eq}\} \quad (18)$$

and

$$R^{(3)}(t_3,t_2,t_1) = \left(\frac{i}{\hbar}\right)^3\mathrm{Tr}\{[\hat{\mu}(t_3),[\hat{\mu}(t_2),[\hat{\mu}(t_1),\hat{\mu}(0)]]]\hat{\rho}_{tot}^{eq}\} \quad (19)$$

where

$$\hat{\mu}(t) \equiv e^{(i/\hbar)\hat{H}_{tot}t}\mu(\hat{q})e^{-(i/\hbar)\hat{H}_{tot}t}$$

is the Heisenberg representation of $\hat{\mu}$ and

$$\hat{\rho}_{tot}^{eq} = e^{-\beta\hat{H}_{tot}}/\mathrm{Tr}e^{-\beta\hat{H}_{tot}}$$

with $\beta = 1/k_B T$. Note that the δ-pulse approximation is only valid if the rotating wave approximation is made for the response function. The spectrum calculated here contains nonrotating wave beams. Using the hyperoperator notations,

$$\hat{\mathcal{O}}^{\times}\hat{f} \equiv \hat{\mathcal{O}}\hat{f}-\hat{f}\hat{\mathcal{O}} \quad (20)$$

for any operators $\hat{\mathcal{O}}$ and $\hat{f}$, and writing $\mu(\hat{q}) = \hat{\mu}$, we can simply recast eq 18 and eq 19 as[33,67]

$$R^{(1)}(t_1) = \mathrm{Tr}\left\{\hat{\mu}\hat{\mathcal{G}}(t_1)\frac{i}{\hbar}\hat{\mu}^{\times}\hat{\rho}_{tot}^{eq}\right\} \quad (21)$$

and

$$R^{(3)}(t_3,t_2,t_1) = \mathrm{Tr}\left\{\hat{\mu}\hat{\mathcal{G}}(t_3)\frac{i}{\hbar}\hat{\mu}^{\times}\hat{\mathcal{G}}(t_2)\frac{i}{\hbar}\hat{\mu}^{\times}\hat{\mathcal{G}}(t_1)\frac{i}{\hbar}\hat{\mu}^{\times}\hat{\rho}_{tot}^{eq}\right\} \quad (22)$$

where $\hat{\mathcal{G}}(t)$ is the Liouville space propagator defined by

$$\hat{\mathcal{G}}(t)\hat{f} = e^{-(i/\hbar)\hat{H}_{tot}t}\hat{f}e^{(i/\hbar)\hat{H}_{tot}t}$$

for any operator $\hat{f}$.

The above expressions allow us to employ the equations of motion to calculate the response functions and give us an intuitive picture of higher-order optical processes. Here, we illustrate this point for the third-order IR response. The right-hand side of eq 22 can be read from right to left as follows. The total system is initially in the equilibrium state $\hat{\rho}_{\rm tot}^{\rm eq}$. The initial state is then modified by the first laser pulse via the dipole operator as $i(\hat{\mu}^{\times}\hat{\rho}_{\rm tot}^{\rm eq}/\hbar$ at $t = 0$ and is propagated for time t_1 by $\hat{\mathcal{G}}(t_1)$. In the third-order IR measurements, the system is excited by the second and third dipole interactions, expressed as $i\hat{\mu}^{\times}/\hbar$ separated by the time propagator $\hat{\mathcal{G}}(t_2)$. After these excitations, the system is further propagated for the time period t_3 by $\hat{\mathcal{G}}(t_3)$ and, finally, the expectation value of the dipole moment at $t = t_1 + t_2 + t_3$ is obtained by calculating the trace of $\hat{\mu}$. We express the time propagator by Green's function for the total system; however, in practice we can trace over the heat−bath part from eq 1 and can replace it with the propagator for the reduced equations of motion.[33] The sequence of modifying and propagating the density matrix can be translated conveniently in the Wigner representation, as illustrated in refs 67 and 33. In this way, the hierarchy of the equations of motion, eqs 6−13, eq A.6, eq A.1, or eqs 14− 17, were used to investigate the roles of LL+SL interactions on the first- and third-order IR signals for arbitrary potentials.[32−40]

The linear absorption and two-dimensional spectra are then given by

$$S(\omega) \equiv \mathrm{Im}\int_0^{\infty} \mathrm{d}t_1 e^{i\omega t_1} R^{(1)}(t_1) \tag{23}$$

and

$$I(\omega_3, t_2, \omega_1) \equiv \int_0^{\infty} \mathrm{d}t_1 \int_0^{\infty} \mathrm{d}t_3 e^{i\omega_1 t_1 + i\omega_3 t_3} R^{(3)}(t_3, t_2, t_1) \tag{24}$$

respectively. In this paper, we have limited our analysis to the third-order IR spectrum for fixed $t_2 = 0$.

4. NUMERICAL CALCULATIONS

From here on, we use the dimensionless coordinate and momentum defined by $\hat{q}/(\hbar/m\omega_c)^{1/2} \rightarrow \hat{q}$ and $\hat{p}/(m\hbar\omega_c)^{1/2} \rightarrow \hat{p}$, respectively, where ω_c is the characteristic frequency of the system. The SL coupling strength is then replaced by $V_{\rm SL}/(m\omega_c/\hbar)^{1/2} \rightarrow V_{\rm SL}$. Although we can deal with any form of potential, here we consider the Morse potential system, as has been studied from a variety of approaches.[67−69] For the dissociation energy D_e and the curvature α, the Morse potential is expressed as

$$U(\hat{q}) = D_e(1 - e^{-\alpha\hat{q}})^2 \tag{25}$$

The vth eigenenergy of the Morse oscillator systems is given by

$$\hbar\omega_v = \hbar\omega_c\left[\left(v+\frac{1}{2}\right) - \frac{\hbar}{2m\omega_c}\alpha^2\left(v+\frac{1}{2}\right)^2\right] \tag{26}$$

where $\omega_c = (2D_e\alpha^2/m)^{1/2}$. Then the anharmonicity $\Delta_{\rm anh} \equiv \omega_{10} - \omega_{21}$ and the fundamental frequency ω_{10} of Morse potential are given by $\Delta_{\rm anh} = \hbar\alpha^2/m$ and $\omega_{10} = \omega_c - \Delta_{\rm anh}$, respectively. We set $\omega_{10} = 1600\ \mathrm{cm}^{-1}$ ($2\pi/\omega_{10} = 20.8$ fs) and $\Delta_{\rm anh} = 16\ \mathrm{cm}^{-1}$ ($\Delta_{\rm anh}/\omega_{10} = 0.01$), both of which are the typical values for intramolecular vibrational motion in the condensed phase such as Amide-I mode in peptides. The heat bath temperature is set to be $T = 300$ K, which means that the system is in a quantum regime ($\beta\hbar\omega_{10} = 7.67$). The system parameters are the same as those used previously to compare numerically exact calculations with stochastic theory.[39] In the following, we consider the eight cases of the LL and/or SL interactions set by the dimensionless LL and SL parameters $V_{\rm LL}^2 = \zeta_{\rm LL}/\omega_{10}$ and $V_{\rm SL}^2 = \zeta_{\rm SL}/\omega_{10}$. The first four cases are for weak coupling, namely, (i) LL ($\zeta_{\rm LL} = 0.05\omega_{10}$ and $\zeta_{\rm SL} = 0$), (ii) SL ($\zeta_{\rm LL} = 0$ and $\zeta_{\rm SL} = 0.05\omega_{10}$), (iii) LL+SL ($\zeta_{\rm LL} = \zeta_{\rm SL} = 0.05\omega_{10}$), and (iv) −LL+SL ($-\zeta_{\rm LL} = \zeta_{\rm SL} = 0.05\omega_{10}$), while the last four cases are for strong coupling, namely, (v) strong LL ($\zeta_{\rm LL} = \omega_{10}$ and $\zeta_{\rm SL} = 0$), (vi) strong SL ($\zeta_{\rm LL} = 0$ and $\zeta_{\rm SL} = \omega_{10}$), (vii) strong LL+SL ($\zeta_{\rm LL} = \zeta_{\rm SL} = \omega_{10}$), and (viii) strong −LL+SL ($-\zeta_{\rm LL} = \zeta_{\rm SL} = \omega_{10}$). For each calculation of (i−iv), the inverse noise correlation times are chosen to be the fast, intermediate, and slow cases set by $\gamma = 0.5\omega_{10}$, $0.1\omega_{10}$, and $0.02\omega_{10}$, respectively, while for (v−viii), the inverse noise correlation is fixed to be the slow case by $\gamma = 0.02\omega_{10}$. The equations of motion were integrated numerically using the fourth-order Runge−Kutta method for the time development. The quantum calculations were examined both by Wigner space representation eqs 6−13 and the energy eigenstate representation eqs A.1−A.6. In the present high-frequency case, we found that the latter equations were more efficient in carrying out the calculations, and so we used them for most of quantum calculations, while the Wigner representation eqs 14−17 was used for all of the classical calculations.

In the energy eigenstate case, we utilized the lowest four to seven energy eigenstates for the description of the quantum system. The time step for the finite difference expression for $\partial\hat{\rho}_{j_1,\ldots,j_K}^{(n)}/\partial t$ was chosen between $\delta t = (2\pi/\omega_{10}) \times 1/16$ and $\delta t = (2\pi/\omega_{10}) \times 1/80$. We selected the depth of the hierarchy and the number of Matsubara frequencies as $N = 3−20$ and $K = 1−9$, respectively. The accuracy of the calculations was examined by changing the number of eigenstates and the values of δt, N, and K.

The classical calculations and some of the quantum calculations were carried out using a discrete mesh in the Wigner space representation. The mesh size was varied from $N_q \times N_p = 90 \times 90$ to 360×360 with mesh ranges from $-4 < q < 4$ and $-4 < p < 4$ to $-6 < q < 6$, and $-6 < p < 6$. Depending on the position in phase space, we implemented either the left-hand difference scheme or the right-hand difference scheme for $\partial W/\partial p$ or $\partial W/\partial q$ in Liouvillian operator.[61] Here, we employ the difference scheme with the third-order accuracy. The time step for the finite difference expression $\partial W/\partial t$ was between $\delta t = (2\pi/\omega_{10}) \times 1/400$ and $\delta t = (2\pi/\omega_{10}) \times 1/6800$. The depth of the hierarchy was selected from $N = 1−5$. The accuracy of the calculations was checked by the same way as the quantum case.

5. QUANTUM AND CLASSICAL SIMULATIONS FOR LINEAR ABSORPTION SPECTROSCOPY

In this section, we present linear absorption spectra calculated from the quantum and classical hierarchy of equations of motion approaches for the weak (i) LL, (ii) SL, (iii) LL+SL, and (iv) −LL+SL cases, and the strong (v) LL, (vi) SL, (vii) LL+SL, and (viii) −LL+SL cases for a Morse potential. The linear absorption spectra of a harmonic and Morse oscillator system with LL and/or SL system−bath interactions have been studied both analytically[45,70,71] and numerically,[33−40] but the role of quantum effects has not been explored.

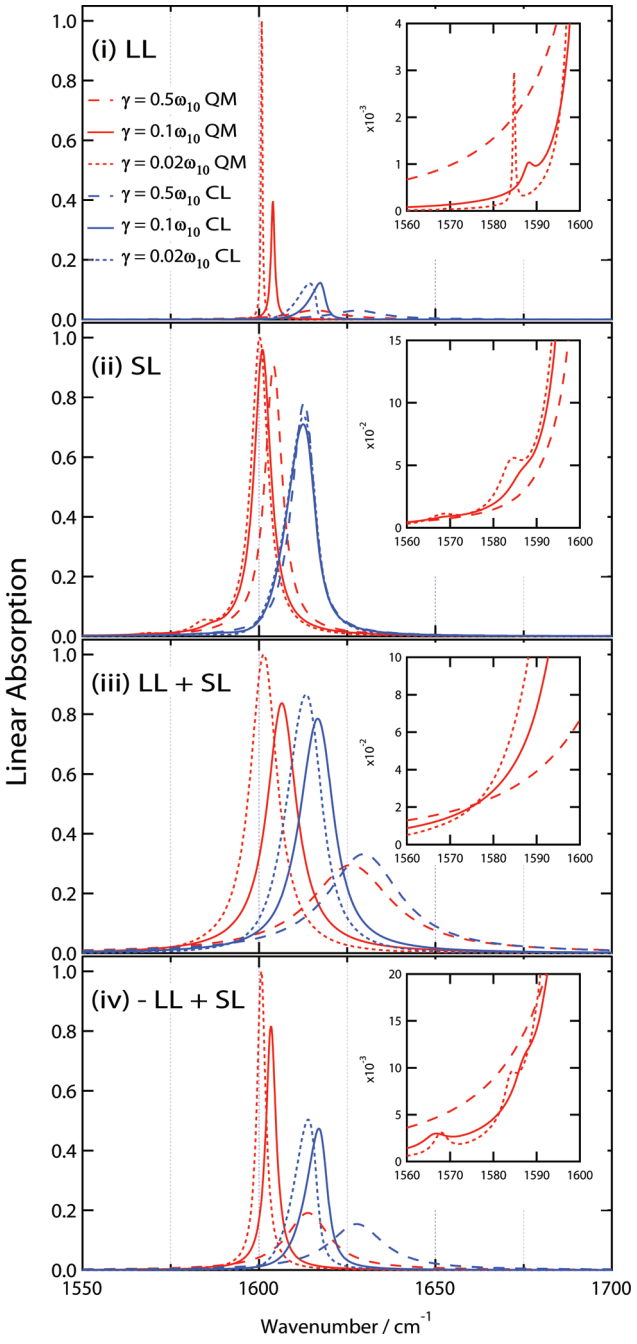

Figure 2. Linear absorption spectra $S(\omega)$ of the Morse oscillator (ω_{10} = 1600 cm^{-1}, Δ_{anh} = 16 cm^{-1}) calculated from the quantum (red) and classical (blue) hierarchy equations of motion for weak coupling cases with $\gamma = 0.5\omega_0$ (dashed lines), $0.1\omega_0$(solid lines), and $0.02\omega_0$ (dotted lines). The panels from the top to bottom show the spectra for (i) LL, (ii) SL, (iii) +LL+SL, and (iv) −LL+SL system−bath coupling cases. We set the bath temperature T = 300 K and the system−bath coupling strength $\zeta = 0.05\omega_{10}$ for the bath. Insets in (i), (ii), and (iv) depict the 1−2 transition peak in the quantum case.

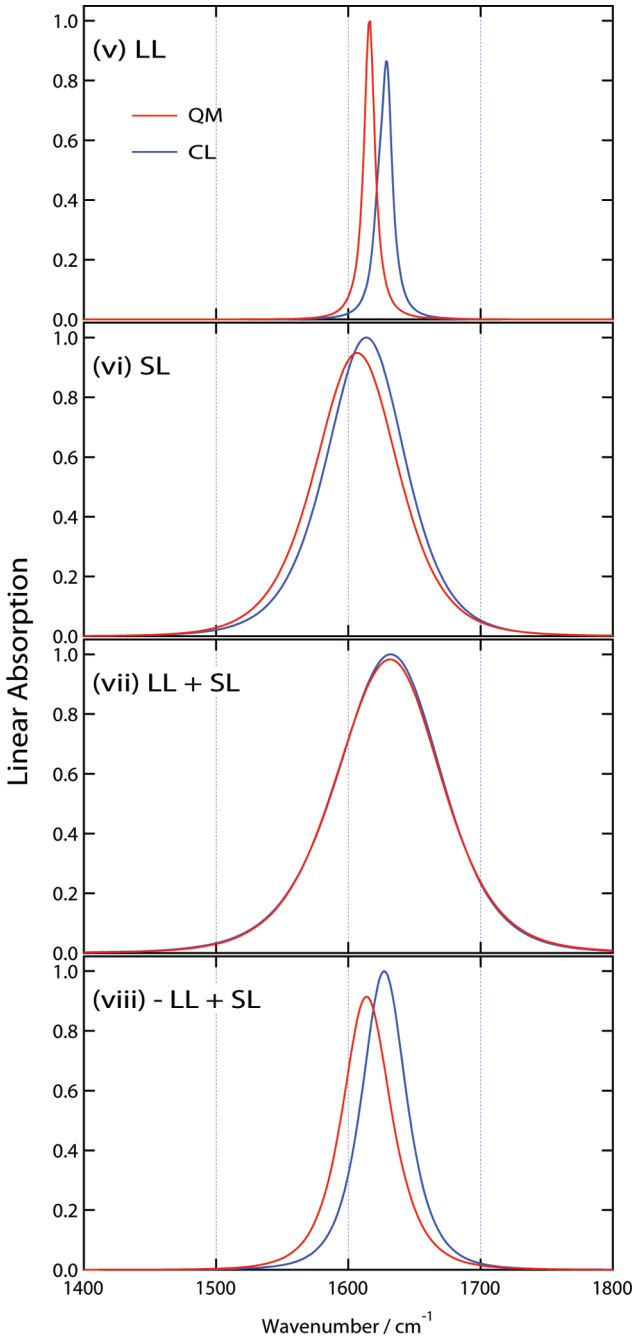

Figure 3. Linear absorption spectra $S(\omega)$ of the Morse oscillator (ω_{10} = 1600 cm^{-1}, Δ_{anh} = 16 cm^{-1}) calculated from the quantum (red) and classical (blue) hierarchy equations of motion for strong coupling cases with $\gamma = 0.02\omega_0$ (dotted lines). The panels from the top to bottom show the spectra for (v) LL, (vi) SL, (vii) +LL+SL, and (viii) −LL+SL system bath coupling cases. We set the bath temperature T = 300 K and the system−bath coupling strength $\zeta = 0.05\omega_{10}$ for the bath.

In Figure 2, the linear absorption spectra calculated from the quantum (red) and classical (blue) hierarchy of equations of motion are compared for various conventions of the weak LL and SL couplings with different inverse noise correlation times $\gamma = 0.5\omega_{10}$ (dashed lines), $0.1\omega_{10}$ (solid lines), and $0.02\omega_{10}$ (dotted lines). Note that there is also a 0−2 transition peak (quantum cases) or overtone peak (classical cases) at ω = 3190 cm^{-1} in all spectra including the strong coupling case in Figure 3 (not shown), but due to the damping, the peak intensity is negligibly small compared with the 0−1 and 1−2 peaks. For reference, we present the linear absorption spectra for the harmonic potential $U(\hat{q}) = m\omega_0{}^2\hat{q}^2/2$ with the fundamental frequency ω_0 = 1600 cm^{-1} in Figure 8 in Appendix B.

dx.doi.org/10.1021/jp1095618 |J. Phys. Chem. A 2011, 115, 4009–4022

Figure 2(i) depicts the weak LL case.[69−71] In both the quantum and classical cases, the peak position shifts to the low frequency (red) side as γ decreases. This is because, in the present system−bath model, the coupling between the bath modes and the system oscillator enhances the effective frequency of the system, which becomes large for a large effective coupling strength $\zeta' = \zeta\gamma^2/(\gamma^2 + \omega_c{}^2)$.[53] Since ζ' becomes small for small γ, the peak shifts to the red. The peak width becomes narrow for small γ in both quantum and classical cases due to the weak damping constant proportional to ζ'. This feature can be clearly seen in the harmonic LL case, where compact analytical expressions of the linear absorption and 2D spectra are available.[70] (See also in Figure 8(i) in Appendix B.) In contrast to the harmonic case, the peak position of the quantum result is lower than the classical one for a fixed γ in the Morse oscillator case. This is because, while the classical motion was governed by the curvature at the bottom of potential ($\partial^2 U(q)/\partial q^2$ with $q = q_{\min}$), the quantum one was affected by the upper part of the potential curvatures due to the nonlocal manner of potential interactions expressed as the second term of the right-hand side in eq 7. This difference may not be called the effect of the zero-point energy, since, in the harmonic case, the classical and quantum results are exactly the same as illustrated in Figure 8(i) even though there is the zero-point energy in the quantum case. A difference appears if the potential is anharmonic, but one may also find such effect by modifying the potential curvature in classical simulations and it may not be easy to identify the frequency shift as a pure quantum effect. In the fast modulation case ($\gamma = 0.5\omega_{10}$), the profiles of quantum and classical mechanically calculated peaks are similar, since the quantum coherence of the system is destroyed by the fast bath modulation then the quantum effects play a minor role. In the intermediate and the slow modulation cases ($\gamma = 0.1$ and $0.02\omega_{10}$), however, the bath modulation is slow compared with the optical detection and we can observe the discretized quantum energy transition as the small 1−2 transition peak about at $\omega = 1590\ \mathrm{cm}^{-1}$ in the quantum case. This is a prominent quantum effect that appears only in quantum mechanically calculated spectra and arises from the anharmonicity of the potential or nonlinearity of the system−bath coupling.

Figure 2(ii) shows the results for the SL case.[34−36,45] While the peak position does not change for γ in the classical case, the peak shifts to the red for small γ in the quantum anharmonic case. Similar to the LL interaction, the most prominent difference between the quantum and classical results is the existence of the 1−2 transition peak at $1585\ \mathrm{cm}^{-1}$ for small γ. The tendency of peak shift in the present case is opposite to the harmonic case, where the analytical expression of the absorption spectrum is obtained.[45] As shown in Appendix B, when the system is harmonic, the 1−2 transition peaks does not appear and the only quantum effect is the blue shift. This indicates that the SL interaction enhances the contribution from the anharmonicity of potential through the 1−2 transition. Thus as the effective SL coupling strength ζ' decreases for small γ, the peak shifts to the red as the LL case. The width of the peak becomes narrower in the quantum case

Spectra (iii) and (iv) of Figure 2 show the spectra for the weak LL+SL and −LL+SL cases, respectively. When the LL and SL interactions are combined, there are two patterns of the potential deformation and the modulation depends on the relative phase between the LL and SL interactions.[36,37] Since the Morse potential is asymmetric and is spread to the positive direction, the effect that arises from the LL and SL interactions is also asymmetric. Thus, the amplitude of frequency fluctuation becomes large for the LL+SL case, but small for the −LL+SL case as illustrated in Figures 1(iii,iv). As a result, the peak width becomes larger in the LL+SL case than in the −LL+SL case, while the peak shift in the −LL+SL case is larger than in the LL+SL case, reflecting the magnitude of the anharmonicity. The 1−2 transition peak cannot be observed in the LL+SL case due to large frequency fluctuations.

In Figure 3, the linear absorption spectra are compared for conventions of strong LL and SL couplings with the fixed $\gamma = 0.02\omega_{10}$. As illustrated in Figure 1, the LL interaction mainly contributes to energy relaxation, whereas the SL interaction mainly leads to the vibrational dephasing for the slow modulation case due to the frequency fluctuations. With the exception of the LL case in Figure 3(v), in this strong coupling with slow modulation case, the profiles of the spectra become Gaussian, while all of the spectra in Figure 2 are more or less Lorentzian. In each figure, the quantum spectrum exhibits a similar profile to the classical one beside the small frequency shift because the quantum coherence created by the laser excitation is destroyed by the strong bath modulation. Although the absence of the 1−2 peak may be caused by the large broadening of the 0−1 and 1−2 transition peaks, this is not the case in the present study as will be illustrated in the next section by multidimensional spectra.

6. QUANTUM AND CLASSICAL SIMULATIONS FOR TWO-DIMENSIONAL SPECTROSCOPY

The difference in the relaxation mechanism between quantum and classical dynamics becomes prominent in the third-order IR response. In the LL model the third-order response function for the harmonic system vanishes when the dipole operator depends only linearly on the coordinate because the different Liouville space pathways interfere destructively with each other.[70] Thus, the anharmonicity of the system is essential to have a third-order signal.[78] If the SL interaction is present, the signal appears even in the harmonic system, since the interference between the different Liouville paths is disturbed due to the frequency fluctuation nature of the SL interaction and the interference is partly canceled.[34,35]

While 2DIR spectroscopy often utilizes correlation spectra,[72−74] we display the response function for fixed $t_2 = 0$ calculated from eq 24 with eq 22 as the 2D signal, since, in the classical case, it is not easy to select the Liouville pathways that contribute to a given phase-matched signal.[75−77]

First we illustrate the weak coupling case for the various conventions of the LL and SL interactions. In Figures 4, 5, and 6, we plot (a) the absolute values and (b) the imaginary parts of the quantum and classical response functions in the weak (i) LL, (ii) SL, (iii) LL+SL, and (iv) −LL+SL cases for $\gamma = 0.5$, 0.1, and $0.02\omega_{10}$, respectively. Each figure is normalized by the absolute value of the maximum peak intensity, and the spacing between the contour is set to 0.2.

Figure 4 illustrates the quantum and classical third-order response functions for the fast modulation case $\gamma = 0.5\omega_{10}$. Compared with those in the classical results, the peaks in quantum results shift to low frequency (red) direction, while the classical and quantum signal profiles are similar. This is because the fast bath modulation arising from the heat-bath eliminates the quantum coherence of the system and thereby the quantum results approach to the classical ones. Note that 2D correlation spectrum is often utilized instead of the imaginary and real part of 2D spectrum obtained from eq 24 in order to

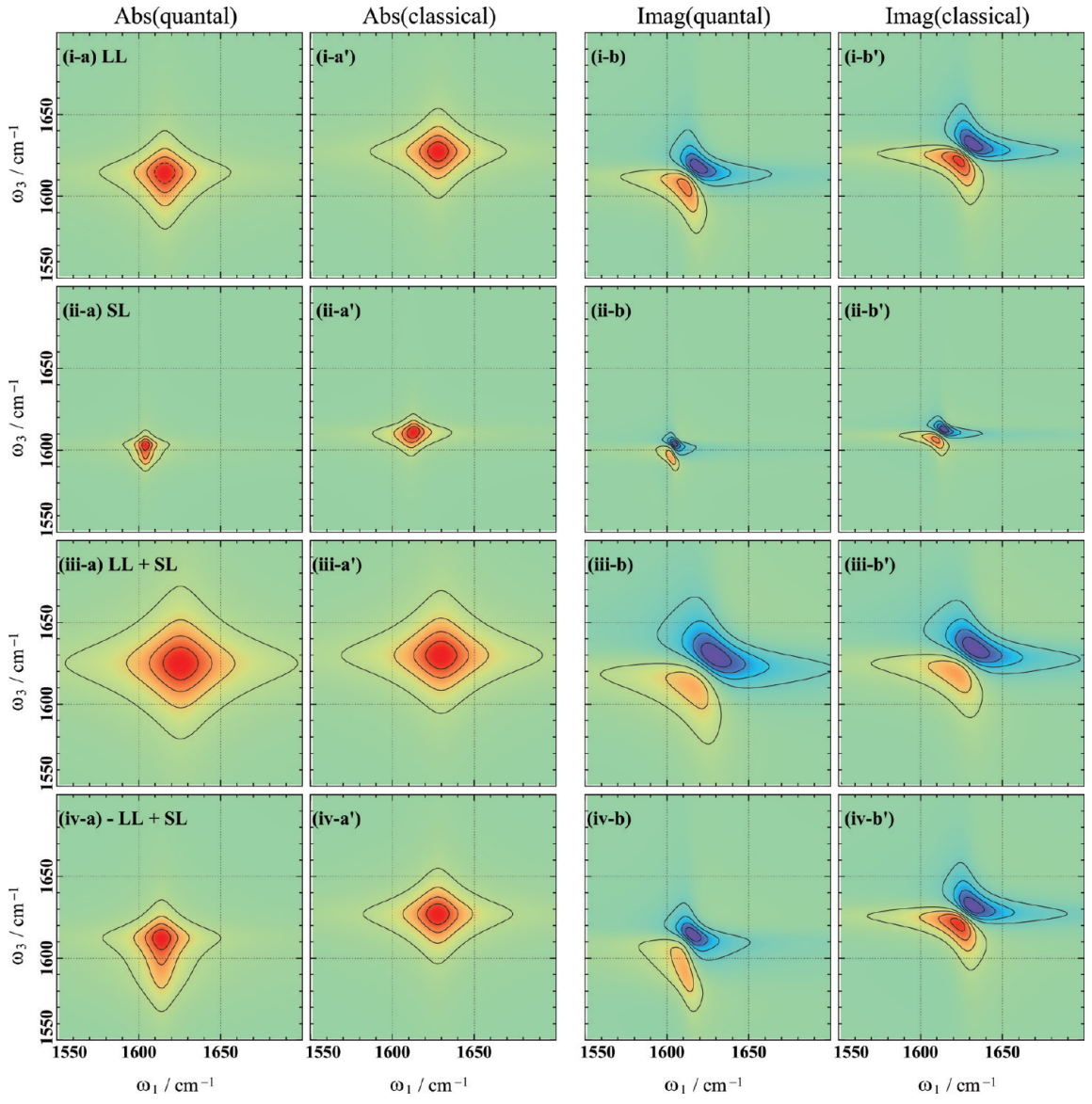

Figure 4. Quantum and classical mechanically calculated 2DIR spectra $I(\omega_3, t_2 = 0, \omega_1)$ of the Morse potential system for a weak coupling case in the motional narrowing regime $\gamma = 0.5\omega_0$. The panels from the top to bottom show the signals for (i) LL, (ii) SL, (iii) +LL+SL, and (iv) −LL+SL system−bath coupling cases. In each case, we plot the (a) quantum and (a′) classical absolute and (b) quantum and (b′) classical imaginary parts of spectra separately. The red contours are positive, whereas the blue contours are negative. Each figure is normalized by the absolute value of the maximum peak intensity. The spacing between the counter is set to be 0.2.

investigate a role of dephasing in the $0 \rightarrow 1 \rightarrow 0$ and $0 \rightarrow 1 \rightarrow 2$ transitions in the spectrum contour plot.[72−74] The negative and the positive peaks in the imaginary part in Figure 4 approximately correspond, respectively, to the $0 \rightarrow 1 \rightarrow 0$ and $0 \rightarrow 1 \rightarrow 2$ transitions peak positions in the correlation spectrum;[39] however, such an interpretation is misleading in the classical case as well as in the quantum case if the bath modulation is fast, where the discretized quantum energy states are smeared, as depicted in Figure 2. The positive and negative parts of the correlation spectra in the classical case should be interpreted, respectively, as the high-frequency emission and low-frequency absorption of light from the anharmonic potential. Although the classical and quantum profiles of the 2D signals are similar, there are some differences due to the sensitivity of the 2D spectrum. In the quantum SL and −LL+SL cases shown in panels (ii-a) and (iv-a) of Figure 4, the peaks elongate to the low frequency direction of ω_3. As we will see in Figure 5, this elongation arises from the $0 \rightarrow 1 \rightarrow 2$ transition. While it is hard to observe the $1 \rightarrow 2$ transition in linear spectra, we can catch it as the elongation of the peak in ω_3 direction in 2D spectroscopy.

Figure 5 shows our results for the intermediate modulation case $\gamma = 0.1\omega_{10}$. In the quantum case depicted in parts a and b of Figure 5, we can clearly see the twin peaks arising from $0 \rightarrow 1 \rightarrow 0$ and $0 \rightarrow 1 \rightarrow 2$ transitions at $(\omega_1,\omega_3) = (1600,1600)-(1605,1605)\ \mathrm{cm}^{-1}$ and $(\omega_1,\omega_3) = (1600,1585)-(1605,1590)\mathrm{cm}^{-1}$, respectively. In the classical case depicted in parts a′ and b′ of Figure 5, on the other hand, the profiles of the peaks are more or less similar to those in parts a′ and b′ of Figure 4, although each peak becomes narrower and the position of the peak shifts to the red for the present small γ case, as was observed in Figure 2. The difference between the classical and quantum results indicates that one cannot reproduce the 2D spectrum from classical calculations if the system temperature

dx.doi.org/10.1021/jp1095618 |J. Phys. Chem. A 2011, 115, 4009–4022

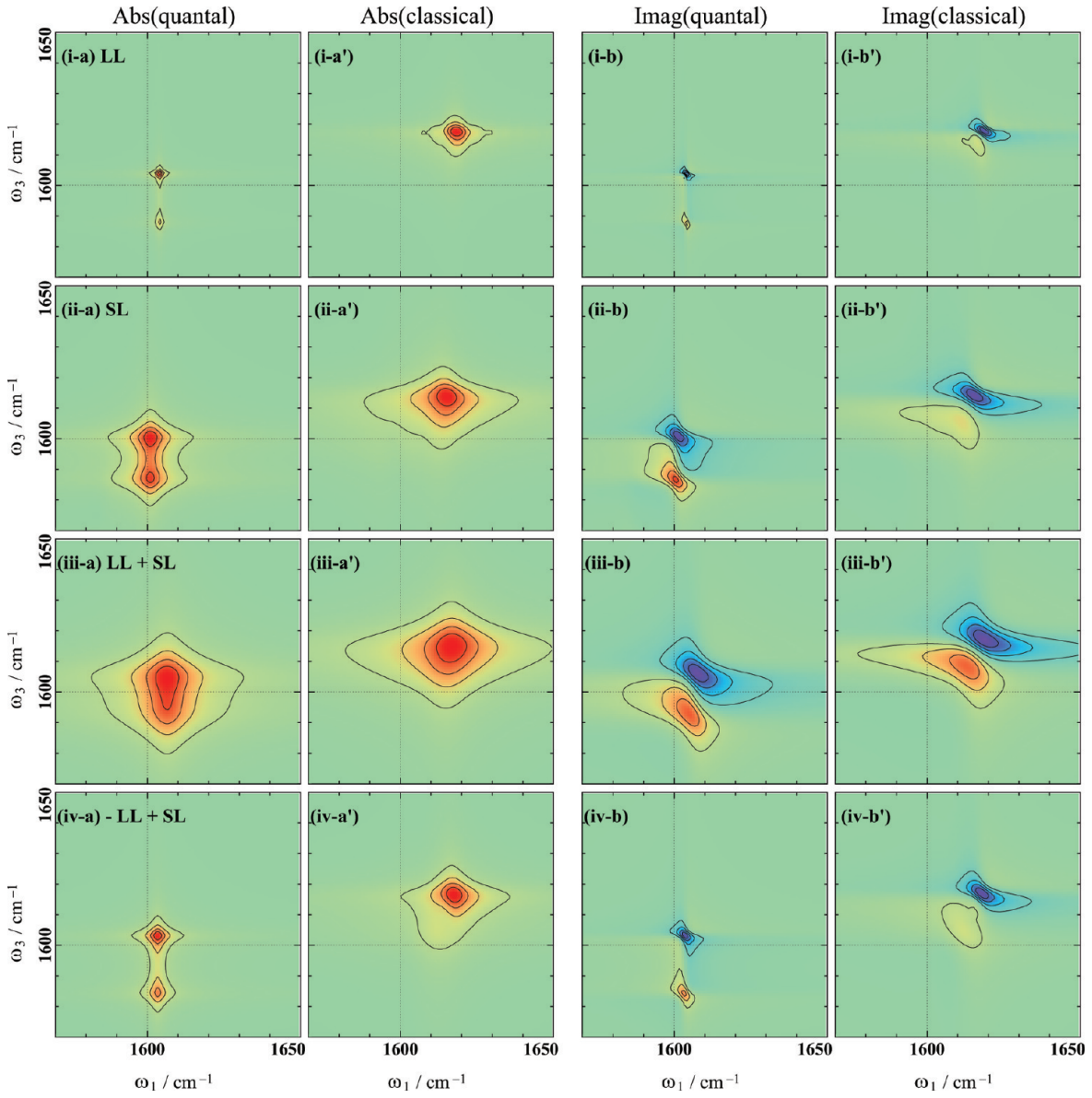

Figure 5. Quantum and classical mechanically calculated 2DIR spectra $I(\omega_3, t_2 = 0, \omega_1)$ of the Morse potential system for a weak coupling case in the intermediate modulation regime $\gamma = 0.1\omega_0$. We plot the (a) quantum and (a′) classical absolute and (b) quantum and (b′) classical imaginary parts of spectra separately in the (i) LL, (ii) SL, (iii) LL+SL, and (iv) −LL+SL cases.

is in the quantum regime ($\beta\hbar\omega_{10} \gg 1$) and the bath modulations are weak ($\zeta = 0.05\omega_{10}$) and slow ($\gamma \ll \omega_{10}$). The anharmonicity of the potential Δ_{anh} is also important to predict the quantum effects. If the system is close to harmonic, we may neglect the quantum contribution, since the classical and quantum Liouvillian in eq 7 and eq 15, respectively, become identical for the harmonic potential.

Figure 6 illustrates the slow modulation case $\gamma = 0.02\omega_{10}$. Since the contribution of the LL interaction is mainly the frequency fluctuation rather than the energy relaxation in the present case and the amplitude of frequency fluctuations is small compared to the SL case, the spectral peaks in Figure 6(i-a) and Figure 6(i-b) are very sharp. While the profiles of 2D peaks in Figures 4 and 5 are star shaped, reflecting the Lorentzian nature of bath modulation, the center of the peaks in Figure 6 approaches a circular shape, reflecting the vibrational echo nature of slow bath modulation.[72−74] This is because, in the quantum case, the characteristic time scale of bath becomes too slow compared with the time scale of the Morse system, as determined by the difference between the discretized energy states ($\gamma \ll \omega_{10}$), and so the dissipative contribution of LL and/or SL interactions can be neglected. Thus, the peaks corresponding to the $0 \rightarrow 1 \rightarrow 0$ and $0 \rightarrow 1 \rightarrow 2$ transitions are clearly observed, although they are spread because of the pure dephasing induced by the frequency fluctuation. In the classical case in Figure 6a′ and Figure 6b′, on the other hand, the energy of the system is continuous and the system energy can always dissipate to the bath, resulting in the dispersed single resonant peak.

Figure 7 illustrates the strong (v) LL, (vi) SL, (vii) LL+SL, and (viii) −LL+SL coupling cases for the slow modulation ($\gamma = 0.02\omega_{10}$). Cases vi−viii induced by SL interactions are known as the pure dephasing regime. The 2D spectra become circular in shape due to the strong vibrational dephasing. This is the case where IR photon echo peaks are observed in 2D correlation

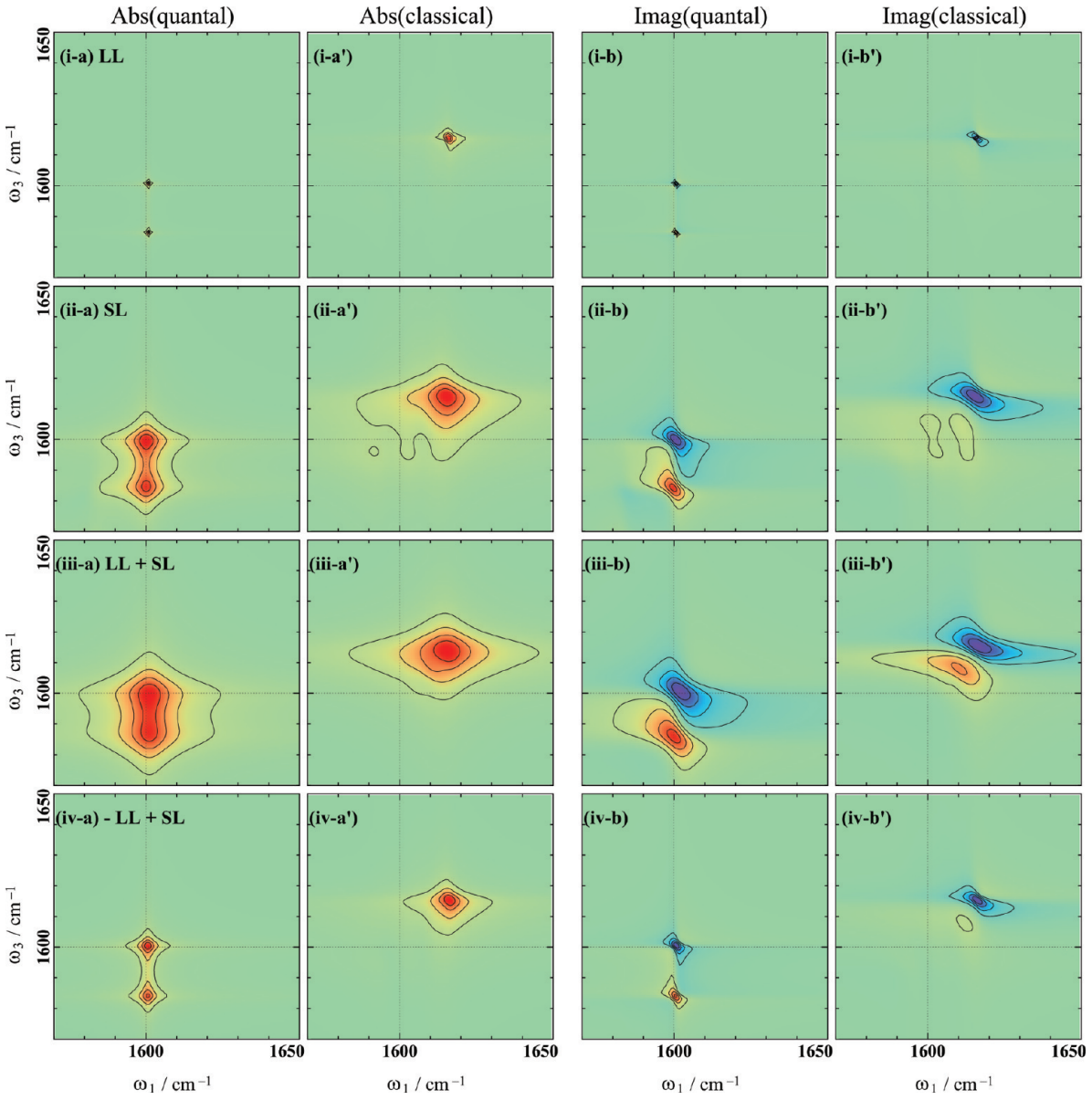

Figure 6. Quantum and classical mechanically calculated 2DIR spectra $I(\omega_3, t_2 = 0, \omega_1)$ of the Morse potential system for a weak coupling case in the weak spectral diffusion regime $\gamma = 0.02\omega_0$. The panels from the top to bottom show the signals for (i) LL, (ii) SL, (iii) +LL+SL, and (iv) −LL+SL system−bath coupling cases. In each case, we plot (a) quantum and (a′) classical absolute and (b) quantum and (b′) classical imaginary parts of spectra separately in the (i) LL, (ii) SL, (iii) LL+SL, and (iv) −LL+SL cases.

spectrum and, as shown by correlation spectra for a case $\gamma = 0.005\omega_{10}$ in ref 39, the multistate stochastic three-state model used to analyze 2D IR echo experiments[16−26] works very well in reproducing the spectrum from a quantum mechanically treated Morse potential model with the LL and/or SL interaction. As observed in Figure 3 with the absence of the 1−2 transition peak, the quantum effect plays a minor role in the strong and slow modulation case due to the destruction of a quantum coherence by the strong bath modulation. The negative peak positions in Figure 7(v-b)−(viii-b) clearly indicate that the negative peaks are of classical anharmonicity origin instead of the 0−1−2 transition origin.

7. CONCLUSION

A Morse potential system nonlinearly coupled to a heat-bath was employed to analyze the roles of thermal excitation, relaxation, and spectral diffusion in a high-frequency intramolecular vibrational motion. Numerically accurate linear absorption and two-dimensional infrared spectra were calculated from the reduced hierarchy equations of motion approach in the non-perturbative, non-Markovian, and nonsecular regime of system−bath interactions that is necessary to account for the effect of spectral diffusion at finite temperature. The quantum and classical results calculated under the same physical conditions were compared in the quantum regime ($\beta\hbar\omega_0 \gg 1$) to identify the role of quantum mechanics in linear and two-dimensional spectra.

We summarize the differences between the quantum and classical simulation results for an anharmonic potential with the following four remarks. (1) In the fast bath modulation with weak LL and/or SL coupling (or motional narrowing) case

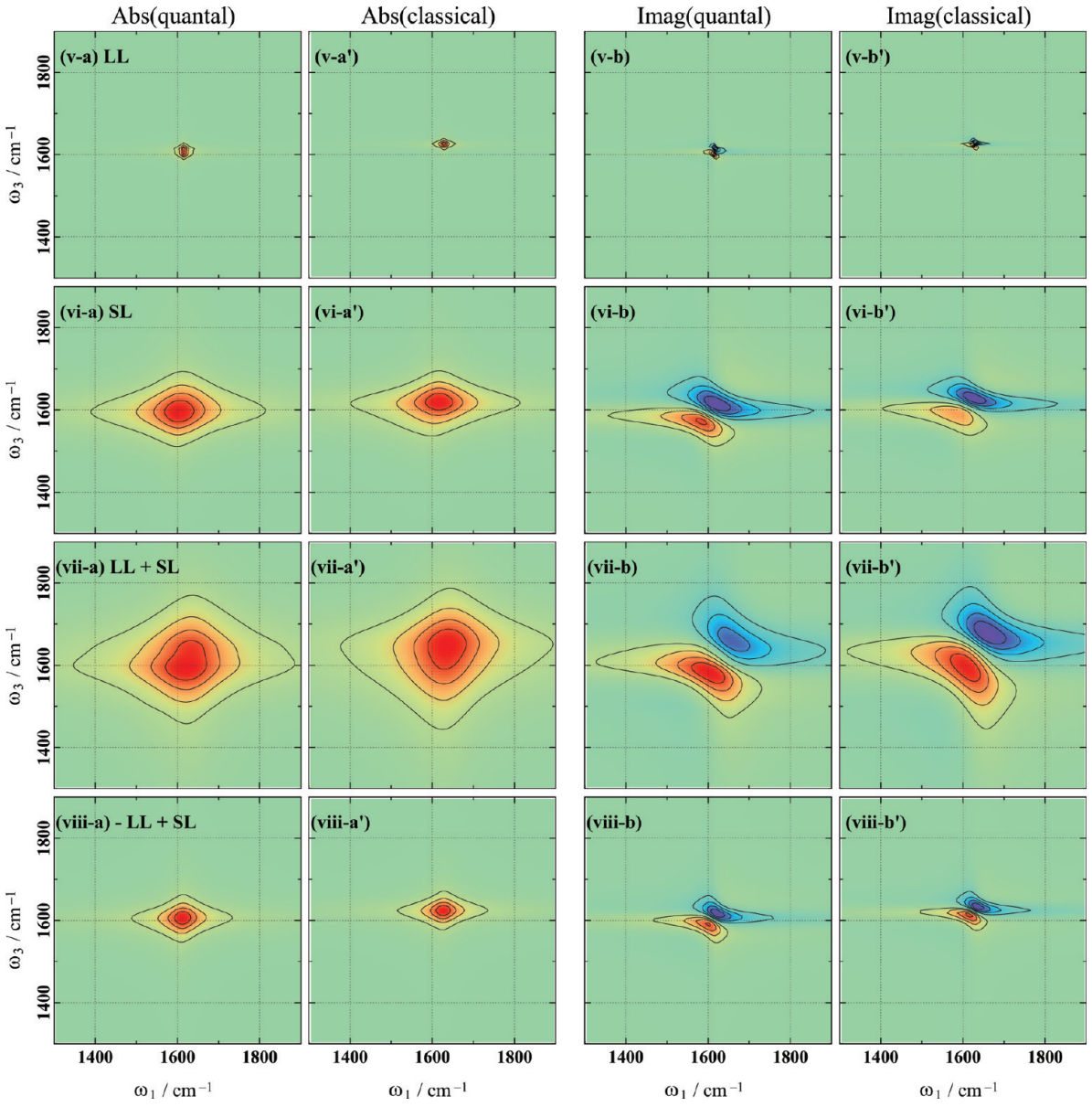

Figure 7. Quantum and classical mechanically calculated 2DIR spectra $I(\omega_3,t_2 = 0,\omega_1)$ of the Morse potential system for a strong coupling case in the spectral diffusion regime $\gamma = 0.02\omega_0$. In each case, we plot the (a) quantum and (a′) classical absolute and (b) quantum and (b′′) classical imaginary parts of spectra separately in the (v) LL, (vi) SL, (vii) LL+SL, and (viii) −LL+SL cases.

(Figure 4), the profiles of linear and 2D spectra calculated from the classical and quantum equations are similar besides the frequency shifts which arise from the nonlocal nature of quantum potential interactions. (2) For the intermediate modulation with weak LL and/or SL coupling case (Figure 5), while linear and 2D spectra are similar to the fast modulation case in the classical results, the peak profile becomes very different especially for quantum 2D spectra. Two separate peaks appear corresponding to the $0 \rightarrow 1 \rightarrow 0$ and $0 \rightarrow 1 \rightarrow 2$ transitions; the peak splitting corresponds to the anharmonicity in the potential. (3) In the slow modulation with weak LL and/or SL coupling case (Figure 6),[39] classical results exhibit a single resonant peak. In contrast, the two $0 \rightarrow 1 \rightarrow 0$ and $0 \rightarrow 1 \rightarrow 2$ transition peaks become prominent in the quantum results. (4) In the slow modulation with strong LL and/or SL coupling case (Figure 7), where the quantum results are well reproduced by the multilevel stochastic theory,[39] the quantum and classical results are very similar due to the strong destruction of quantum coherence because of strong modulation and both results exhibit a single resonant peak. Due to the spectral diffusion, all quantum and classical peaks approach a circular shape, contrary to the star shape in the fast or intermediate modulation cases. We should also notice that when a vibrational mode is close to harmonic, the quantum effects are rather minor. In the harmonic case, a 2D signal arises due to the nonlinearlity of the dipole operator or vibrational dephasing as a result of the SL interaction.[34−37]

Although we restricted our analysis to a single Morse oscillator mode, a similar conclusion is likely to be obtained for a multimode system with any anharmonicity and anharmonic couplings. We may expect the statements above to be valid under general conditions. Since accurate quantum MD simulations of linear and 2D vibrational spectra for a complex molecular system are

not at hand, we are restricted to classical MD simulations to analyze experimental results. However, our results clearly indicate that the spectra obtained by a classical simulation cannot account for the quantum anharmonic effects arising from the $1 \rightarrow 2$ transition.

To compensate for the difference between the classical and quantum results, we therefore have to employ a single or multianharmonic oscillator model for targeting vibrational modes like a model shown in the present paper based on the classical simulation. We then chose the LL and SL interactions parameters to fit the linear and multidimensional spectra obtained from the classical MD simulation by solving the classical hierarchy equations of motion eqs 14−17. For a multimode system, we may need to employ multiple bath modes with different bath operators.[40] The quantum linear and multidimensional spectra can be obtained by solving the quantum hierarchy equations of motion eqs A.1−A.6 using the same potential and bath parameters for the classical hierarchy equations of motion. The calculated peak position should be different if the classical MD simulation employed a phenomenological potential to fit experimental data instead of using a potential calculated from molecular orbital (MO) theories. Although indirect, this is the only practical way to calculate multidimensional vibrational spectra based on MD simulation for a complex molecular system in a condensed environment.

APPENDIX A: REDUCED QUANTUM HIERARCHY EQUATIONS OF MOTION IN DENSITY MATRIX REPRESENTATION

In terms of the Liouville space operators, the quantum Fokker−Planck equation with low-temperature correction term is expressed as[39,55]

$$\frac{\partial}{\partial t}\hat{\rho}^{(n)}_{j_1,\ldots,j_K}(t) = -[i\hat{\mathscr{L}} + n\gamma + \sum_{k=1}^{K} j_k\nu_k + \hat{\Xi}']\hat{\rho}^{(n)}_{j_1,\ldots,j_K}(t) - \hat{\Phi}[\hat{\rho}^{(n+1)}_{j_1,\ldots,j_K}(t) + \sum_{k=1}^{K}\hat{\rho}^{(n)}_{j_1,\ldots,j_k+1,\ldots,j_K}(t)] - n\gamma\hat{\Theta}_0\hat{\rho}^{(n-1)}_{j_1,\ldots,j_K}(t) - \sum_{k=1}^{K} j_k\nu_k\hat{\Theta}_k\hat{\rho}^{(n)}_{j_1,\ldots,j_k-1,\ldots,j_K}(t) \quad \text{(A.1)}$$

for non-negative integers $n, j_1, \cdots j_K$, where we chose K such that $\nu_K \gg \omega_c$ for Matsubara frequencies $\nu_k = 2\pi k/(\beta\hbar)$. Here, the quantum Liouvillian of the system is $i\hat{\mathscr{L}} \equiv (i/\hbar)\hat{H}^{\times}$ for the system Hamiltonian $\hat{H} = \hat{p}^2/2m + U(\hat{q})$ and $\hat{\Phi}$, $\hat{\Theta}_0$, $\hat{\Theta}_k$, and $\hat{\Xi}'$ are now defined by

$$\hat{\Phi} \equiv \frac{i}{\hbar}\hat{V}^{\times}(\hat{q}) \quad \text{(A.2)}$$

$$\hat{\Theta}_0 \equiv i\frac{m\zeta}{\beta\hbar}\left[-i\frac{\beta\hbar\gamma}{2}\hat{V}^{\circ}(\hat{q}) + \frac{\beta\hbar\gamma}{2}\cot\left(\frac{\beta\hbar\gamma}{2}\right)\hat{V}^{\times}(\hat{q})\right] \quad \text{(A.3)}$$

$$\hat{\Theta}_k \equiv i\frac{m\zeta}{\beta\hbar}\frac{2(\beta\hbar\gamma)^2}{(2\pi k)^2 - (\beta\hbar\gamma)^2}\hat{V}^{\times}(\hat{q}) \quad \text{(A.4)}$$

and

$$\hat{\Xi}' \equiv \frac{m\zeta}{\beta}\hbar^2\left[1 - \frac{\beta\hbar\gamma}{2}\cot\left(\frac{\beta\hbar\gamma}{2}\right) - \sum_{k=1}^{K}\frac{2(\beta\hbar\gamma)^2}{(2\pi k)^2 - (\beta\hbar\gamma)^2}\right] \times\hat{V}^{\times}(\hat{q})\hat{V}^{\times}(\hat{q}) + i\frac{m\zeta}{\beta\hbar^2}\frac{\beta\hbar\gamma}{2}\hat{V}^{\circ}(\hat{q})\hat{V}^{\times}(\hat{q}) \quad \text{(A.5)}$$

where we introduced the hyperoperators $\hat{\mathscr{O}}^{\times}\hat{f} \equiv \hat{\mathscr{O}}\hat{f} - \hat{f}\hat{\mathscr{O}}$ and $\hat{\mathscr{O}}^{\circ}\hat{f} \equiv \hat{\mathscr{O}}\hat{f} + \hat{f}\hat{\mathscr{O}}$ for any operators $\hat{\mathscr{O}}$ and $\hat{f}$. The terminator eq 13 is now expressed as

$$\frac{\partial}{\partial t}\hat{\rho}^{(n)}_{j_1,\ldots,j_K}(t) = (i\hat{\mathscr{L}} + \hat{\Xi}')\hat{\rho}^{(n)}_{j_1,\ldots,j_K}(t) \quad \text{(A.6)}$$

The quantum Fokker−Planck equations can be deduced from the influence functional method of Feynman and Vernon.[33] While the Fokker−Planck equations in the energy eigenstate representation eq A.1−A.6 utilize the regular influence functional, the Fokker−Planck equations in the Wigner space representation eq 6−13, employ the expression of influence functional with time-integration by parts.[33] Because of this difference, the Fokker−Planck equations in the energy eigenstate representation explicitly include the counterterm, whereas those in the Wigner representation involves the terms proportional to p in eq 10 instead of the counterterm.

APPENDIX B: LINEAR ABSORPTION SPECTRA FOR HARMONIC OSCILLATOR SYSTEM

In this Appendix, we present the numerical results for a harmonic potential system $U_{\text{harm}}(\hat{q}) = m\omega_0^2\hat{q}^2/2$. In this case, the quantum and classical Liouville operators, respectively expressed as eqs 7 and 15, become identical and are given by

$$-\hat{L}_{\text{harm}} = -\frac{p}{m}\frac{\partial}{\partial q} + m\omega_0^2 q\frac{\partial}{\partial p} \quad \text{(B.1)}$$

This indicates that the difference between quantum and classical dynamics in the harmonic case arises from the heat-bath operators which make the system in the corresponding equilibrium state. Here, we chose $\omega_0 = 1600\ \text{cm}^{-1}$. The other parameters are the same as those described for the weak coupling case in sections 5 and 6. In the LL case, the quantum and classical linear absorption spectrum for the Brownian system is expressed as[70]

$$S(\omega) = \frac{\mu^2}{2}\frac{\zeta\gamma^2\omega(\gamma^2+\omega^2)}{(\omega_0^2-\omega^2)^2(\gamma^2+\omega^2)^2 + \zeta^2\gamma^4\omega^2} \quad \text{(B.2)}$$

Spectra in Figure 8 (i) are calculated from the classical and quantum hierarchy equations of motion approaches and agree with the those calculated from the above expression. While the quantum and classical results become identical in the LL case, frequency shifts appear if the SL interaction is presented. This is because the harmonic system coupled to the harmonic bath with the LL interaction is, in principle, the harmonic system and the quantum and classical dynamics of the harmonic system are the same, as is indicated by eq B.1. The peak in the SL case in Figure 8(ii) shifts to the blue in the quantum case, because the SL interaction changes the effective frequency of the potential.[34,35,45] The spectra for ±LL+SL cases in parts (iii) and (iv) of Figure 8 can be explained by adding the LL and SL spectra. Since harmonic potential is symmetric, the calculated linear spectra for ±LL+SL cases are the identical.[36,37] Multidimensional

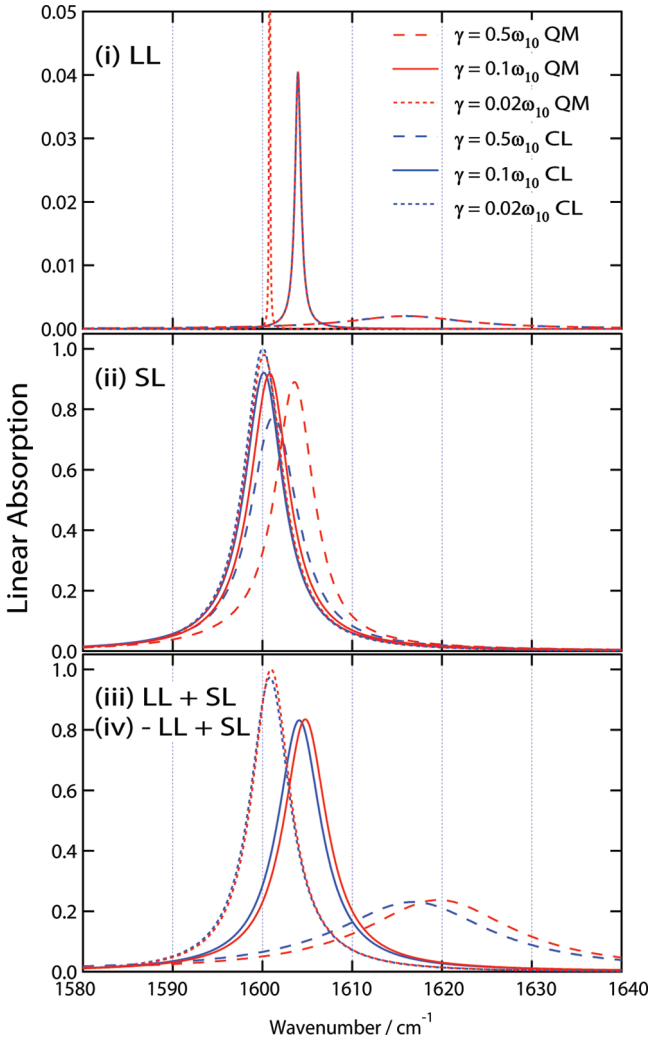

Figure 8. Linear absorption spectra $S(\omega)$ of the harmonic oscillator (ω_0 = 1600 cm^{-1}) calculated from the quantum and classical hierarchy equations of motion (red lines), respectively. The panels from the top to bottom show spectra for (i) LL, (ii) SL, (iii) +LL+SL, and (iv) −LL+SL system bath coupling cases, respectively. We set the bath temperature T = 300 K and the system−bath coupling strength ζ = 0.05ω_0 for the bath.

spectrum of the harmonic system for various LL and/or SL couplings are already reported and we do not present them here.[34−37,70] In the harmonic case, a multidimensional signal arises due to the nonlinearity of dipole operator[70] or vibrational dephasing arises from the SL interaction.[34,37] Thus, the signal profiles as well as the role of LL and/or SL interactions are very different from those for the anharmonic case.

AUTHOR INFORMATION

Corresponding Author

*E-mail: tanimura@kuchem.kyoto-u.ac.jp.

ACKNOWLEDGMENT

The authors thank Taisuke Hasegawa for his valuable suggestions to introduce an efficient algorism for solving the quantum and classical Fokker−Planck equations in the Wigner space. The authors are also thankful to Arend Dijkstra for a critical reading of the manuscript. This work was supported by a Grant-in-Aid for Scientific Research B2235006 from the Japan Society for the Promotion of Science. A.S. is supported by the research fellowship of Global COE Program, International Center for Integrated Research, and Advanced Education in Material Science, Kyoto University.

REFERENCES

(1) Mukamel, S. *Principles of Nonlinear Optical Spectroscopy*; Oxford University Press: New York, 1995.
(2) Mukamel, S.; Tanimura, Y.; Hamm, P. *Acc. Chem. Res.* **2009**, *42*, 1207.
(3) Cho, M.; Fleming, G. R.; Saito, S.; Ohmine, I.; Stratt, R. M. *J. Chem. Phys.* **1994**, *100*, 6672.
(4) Ma, A; Stratt, R. M. *Phys. Rev. Lett.* **2000**, *85*, 1004.
(5) Saito, S.; Ohmine, I. *Phys. Rev. Lett.* **2002**, *88*, No. 20740.
(6) Nagata, Y.; Tanimura, Y. *J. Chem. Phys.* **2006**, *124*, No. 024508.
(7) Jansen, T. L. C.; Snijders, J. G.; Duppen, K. *J. Chem. Phys.* **2000**, *113*, 307.
(8) Hasegawa, T.; Tanimura, Y. *J. Chem. Phys.* **2006**, *125*, No. 074512.
(9) Hasegawa, T.; Tanimura, Y. *J. Chem. Phys.* **2008**, *128*, No. 064511.
(10) Yagasaki, T.; Saito, S. *J. Chem. Phys.* **2008**, *128*, No. 154521.
(11) Yagasaki, T.; Saito, S. *Acc. Chem. Res.* **2009**, *42*, 1250.
(12) Jeon, J; Cho, M. *New J. Phys.* **2010**, *12*, No. 065001.
(13) Cao, J.; Voth, G. A. *J. Chem. Phys.* **1994**, *100*, 5106.
(14) Hanna, G.; Kapral, R. *J. Chem. Phys.* **2008**, *128*, No. 164520.
(15) Rank, J. P.; Kapral, R. *J. Chem. Phys.* **2010**, *132*, No. 074106.
(16) Everitt, K. F.; Geva, E.; Skinner, J. L. *J. Chem. Phys.* **2001**, *114*, 1326.
(17) Cho, M. *J. Chem. Phys.* **2001**, *115*, 4424.
(18) Fourkas, J. T. *Annu. Rev. Phys. Chem.* **2002**, *53*, 17.
(19) Merchant, K. A.; Noid, W. G.; Thompson, D. E.; Akiyama, R.; Loring, R. F.; Fayer, M. D. *J. Phys. Chem. B* **2003**, *107*, 4.
(20) Jansen, T. L. C.; Zhuang, W.; Mukamel, S. *J. Chem. Phys.* **2004**, *121*, 10577.
(21) Jansen, T. L. C.; Hayashi, T.; Zhuang, W.; Mukamel, S. *J. Chem. Phys.* **2005**, *123*, No. 114504.
(22) Torii, H. *J. Phys. Chem. A* **2006**, *110*, 4822.
(23) Sanda, F.; Mukamel, S. *J. Chem. Phys.* **2006**, *125*, No. 014507.
(24) Jansen, T. L. C.; Ruszel, W. M. *J. Chem. Phys.* **2008**, *128*, No. 214501.
(25) Hanna, G.; Geva, E. *J. Phys. Chem. B* **2008**, *112*, 12991.
(26) Kobus, M.; Nguyen, P. H.; Stock, G. *J. Chem. Phys.* **2010**, *133*, No. 034512.
(27) Egorov, S. A.; Everitt, K. F.; Skinner, J. L. *J. Phys. Chem.* **1999**, *103*, 9494.
(28) Sepulveda, M. A.; Mukamel, S *J. Chem. Phys.* **1995**, *102*, 9327.
(29) Jansen, C. J; Mukamel, S *J. Chem. Phys.* **2003**, *119*, 7979.
(30) Noid, W. G.; Erza, G. S.; Loring, R. F. *J. Chem. Phys.* **2004**, *120*, 1491.
(31) Shi, Q.; Geva, E. *J. Chem. Phys.* **2005**, *122*, No. 064506.
(32) Tanimura, Y.; Ishizaki, A. *Acc. Chem. Res.* **2009**, *42*, 1270.
(33) Tanimura, Y. *J. Phys. Soc. Jpn.* **2006**, *75*, No. 082001.
(34) Steffen, T.; Tanimura, Y. *J. Phys. Soc. Jpn.* **2000**, *69*, 3115.
(35) Tanimura, Y.; Steffen, T. *J. Phys. Soc. Jpn.* **2000**, *69*, 4095.
(36) Kato, T.; Tanimura, Y. *J. Chem. Phys.* **2002**, *117*, 6221.
(37) Kato, T.; Tanimura, Y. *J. Chem. Phys.* **2004**, *120*, 260.
(38) Ishizaki, A.; Tanimura, Y. *J. Chem. Phys.* **2005**, *123*, No. 014503.
(39) Ishizaki, A.; Tanimura, Y. *J. Chem. Phys.* **2006**, *125*, No. 084501.
(40) Ishizaki, A.; Tanimura, Y. *J. Phys. Chem. A* **2007**, *111*, 9296.
(41) Sahrapour, M. M.; Makri, N. *J. Chem. Phys.* **2010**, *132*, No. 134506.
(42) Caldeira, A. O.; Leggett, A. J. *Physica A* **1983**, *121*, 587.

(43) Grabert, H.; Schramm, P.; Ingold, G. L. *Phys. Rep.* **1988**, *168*, 115.
(44) Weiss, U. *Quantum Dissipative Systems*; World Scientific: Singapore, 2007.
(45) Okumura, K.; Tanimura, Y. *Phys. Rev. E* **1997**, *56*, 2747.
(46) Oxtoby, D. W. *Annu. Rev. Phys. Chem.* **1981**, *32*, 77.
(47) Bader, J. S.; Berne, B. J. *J. Chem. Phys.* **1994**, *100*, 8359.
(48) Ghosh, P. K.; Barik, D.; Ray, D. S. *Phys. Lett. A* **2007**, *361*, 201.
(49) Ghosh, P.; Shit, A.; Chattopadhyay, S.; Chaudhuri, J. R. *J. Chem. Phys.* **2010**, *132*, No. 244506.
(50) Bhattacharya, S.; Chaudhury, P.; Chattopadhyay, S.; Chaudhuri, J. R. *Phys. Rev. E* **2009**, *80*, No. 041127.
(51) Tanimura, Y.; Kubo, R. *J. Phys. Soc. Jpn.* **1989**, *58*, 101.
(52) Tanimura, Y.; Wolynes, P. G. *Phys. Rev. A* **1991**, *43*, 4131.
(53) Tanimura, Y.; Wolynes, P. G. *J. Chem. Phys.* **1992**, *96*, 8485.
(54) Tanimura, Y. *Phys. Rev. A* **1990**, *41*, 6676.
(55) Ishizaki, A.; Tanimura, Y. *J. Phys. Soc. Jpn.* **2005**, *74*, 3131.
(56) Xu, R.-X.; Cui, P.; Li, X.-Q.; Mo, Y.; Yan, Y.-J. *J. Chem. Phys.* **2005**, *122*, No. 041103.
(57) Xu, R.-X.; Yan, Y.-J. *Phys. Rev. E* **2007**, *75*, No. 031107.
(58) Xu, J.; Xu, R.-X.; Luo, M.; Yan, Y.-J. *Chem. Phys.* **2010**, *370*, 109.
(59) Ishizaki, A.; Tanimura, Y. *Chem. Phys.* **2008**, *347*, 185.
(60) Wigner, E. *Phys. Rev. E* **1932**, *40*, 749.
(61) Frensley, W. R. *Rev. Mod. Phys.* **1990**, *62*, 745.
(62) Coffey, W. T.; Kalmykov, Y. P.; Titov, S. V.; Mulligan, B. P. *Phys. Rev. E* **2007**, *75*, No. 041117.
(63) Cleary, L.; Coffey, W. T.; Kalmykov, Y. P.; Titov, S. V. *Phys. Rev. E* **2009**, *80*, No. 051106.
(64) Hasegawa, T.; Tanimura, Y. Unpublished.
(65) Risken, H. *The Fokker-Planck Equation*, 2nd ed.; Springer: Berlin, 1988.
(66) Gardiner, C. W. *Handbook of Stochastic Methods*; Springer: Berlin, 2004.
(67) Tanimura, Y. *Chem. Phys.* **1998**, *233*, 217.
(68) Toutounji, M. *Int. J. Quantum Chem.* **2009**, *109*, 3399.
(69) Suzuki, Y.; Tanimura, Y. *Phys. Rev.* **1999**, *59*, 1475.
(70) Tanimura, Y.; Mukamel, S. *J. Chem. Phys.* **1993**, *99*, 9496.
(71) Okumura, K.; Tanimura, Y. *J. Chem. Phys.* **1996**, *105*, 7294.
(72) Hybl, J. D.; Ferro, A. A.; Jonas, D. M. *J. Chem. Phys.* **2001**, *115*, 6606.
(73) Ge, N.-H.; Zanni, M. T.; Hochstrasser, R. M. *J. Phys. Chem. A* **2002**, *106*, 962.
(74) Khalil, M.; Demirdoven, N.; Tokmakoff, A. *Phys. Rev. Lett.* **2003**, *90*, No. 047401.
(75) Seidner, L.; Stock, G.; Domcke, W. *J. Chem. Phys.* **1995**, *103*, 3998.
(76) Wolfseder, B.; Seidner, L.; Stock, G.; Domcke, W. *Chem. Phys. Lett.* **1997**, *217*, 275.
(77) Kato, T.; Tanimura, Y. *Chem. Phys. Lett.* **2001**, *341*, 329.
(78) Okumura, K.; Tanimura, Y. *J. Chem. Phys.* **1997**, *106*, 1687.